

JGR Space Physics

RESEARCH ARTICLE

10.1029/2025JA033759

Key Points:

- Particle-in-cell (PIC) models align with ray-tracing models on the propagation path and wave normal angle, but deviate in the amplitude evolution of whistler waves
- PIC models reveal extra substantial wave damping at lower latitudes from nonlinear resonances, especially for intense whistler waves
- Surprisingly, whistler waves experience less damping at higher latitudes due to the newly formed electron plateau/beam

Correspondence to:

Q. Lu and X. Gao,
qmlu@ustc.edu.cn;
gaoxl@ustc.edu.cn

Citation:

Ke, Y., Lu, Q., Gao, X., Ma, J., Ren, J., & Zhou, X. (2025). Whistler wave propagation in a dipole magnetic field: Two-dimensional gcPIC simulations. *Journal of Geophysical Research: Space Physics*, 130, e2025JA033759. <https://doi.org/10.1029/2025JA033759>

Received 17 JAN 2025

Accepted 20 MAR 2025

Whistler Wave Propagation in a Dipole Magnetic Field: Two-Dimensional gcPIC Simulations

Yanguang Ke^{1,2} , Quanming Lu^{1,3} , Xinliang Gao^{1,3}, Jiuqi Ma¹ , Junyi Ren¹ , and Xuan Zhou¹ 

¹CAS Key Lab of Geospace Environment, School of Earth and Space Sciences, University of Science and Technology of China, Hefei, China, ²School of Energy Science and Engineering, Harbin Institute of Technology, Harbin, China, ³CAS Center for Excellence in Comparative Planetology, Hefei, China

Abstract Magnetospheric whistler waves are of fundamental importance in the formation of radiation belts and the generation of diffuse aurorae. Their propagation has been widely studied using satellite observations and numerical simulations because of their direct impact on the interactions with electrons. Although ray-tracing models have elucidated the propagation paths, wave normal angles (WNAs), and linear growth/damping of whistler waves, their nonlinear evolution, requiring kinetic simulation models, still remains unclear. In this study, we utilize gcPIC simulations to study whistler wave propagation in a dipole magnetic field, and compare the results with ray-tracing simulations. Ray-tracing simulations show that a parallel whistler wave gradually becomes oblique and experiences increasing linear damping during its propagation from the magnetic equator to high latitudes. Particle-in-cell simulations display nearly identical propagation paths and WNAs, but the amplitude evolution shows substantial differences. At lower latitudes, whistler waves will experience extra substantial damping compared with ray-tracing results, which is due to nonlinear Landau and cyclotron resonances. This difference becomes more pronounced when the wave amplitude is larger. Surprisingly, at higher latitudes, whistler waves will experience less damping, attributable to the electron plateau/beam distributions resulting from Landau trapping. Our study demonstrates the crucial role of nonlinear resonances and reshaped electron distributions in modeling the evolution of whistler waves in the Earth's magnetosphere.

1. Introduction

Whistler-mode waves, frequently observed in the Earth's magnetosphere, are one of the most intense electromagnetic waves, which play a dominant role in the dynamics of electrons in the Earth's radiation belts (Bortnik & Thorne, 2007; Horne et al., 2005; Summers et al., 2007; Thorne et al., 2010). They are capable of accelerating 100 s keV electrons to relativistic energies in the radiation belt (Reeves et al., 2013; Thorne et al., 2013) and scattering ~ 1 –30 keV electrons into the loss cone that precipitate into the polar upper atmosphere (Gao et al., 2023; Ni et al., 2008; Thorne et al., 2010). Whistler-mode waves, outside the plasmapause, are typically referred to as chorus waves, falling within a frequency range of 0.1 – $0.8 f_{ce}$ (where f_{ce} is the equatorial electron gyrofrequency) and typically divided by a power gap at $\sim 0.5 f_{ce}$ into lower and upper bands (H. Chen, Gao, Lu, Sauer, et al., 2021; Fu et al., 2014; Gao et al., 2019; Li et al., 2011; Omura et al., 2009; Tsurutani & Smith, 1974). Whistler-mode chorus waves exhibit quasi-periodic and discrete rising/falling tones or hiss-like emissions (Gao et al., 2022; Li et al., 2012; Lu et al., 2021), which are associated with nonlinear resonant interactions. It's widely accepted that most of whistler waves are generated near the geomagnetic equator (Lauben et al., 2002; LeDocq et al., 1998; Li et al., 2009; Santolik et al., 2005) via the cyclotron resonance with anisotropic energetic electrons injected into the inner magnetosphere (Anderson & Maeda, 1977; Li et al., 2008; Tsurutani & Smith, 1977). Whistler waves are mainly quasi-parallel waves in their source regions, and they propagate nearly along the background magnetic field (Agapitov et al., 2013; Santolik et al., 2014; Taubenschuss et al., 2016).

The propagation of whistler waves in the Earth's magnetosphere has been extensively studied with satellite observations and numerical simulations for several decades (Agapitov et al., 2011; Artemyev et al., 2016; Bortnik et al., 2007; Katoh, 2014; Ke et al., 2017, 2021; Li et al., 2011; Lu et al., 2019). Satellite statistics have revealed that whistler waves are observed as two wave populations: One population remains quasi-parallel at latitudes up to 30° ; the other part gradually becomes oblique as the latitudes increase (Agapitov et al., 2011, 2013). The quasi-parallel wave population is likely attributable to the ducted propagations of whistler waves, which are trapped by density ducts (R. Chen, Gao, Lu, Chen, et al., 2021; Hanzelka & Santolik, 2019; Ke et al., 2021, 2024; Streltsov &

Bengtson, 2020). The oblique wave population is consistent with the nonducted propagation of whistler waves demonstrated in numerous simulations (Bortnik et al., 2007; Breuillard et al., 2012; Lu et al., 2019). Whistler wave propagation directly impacts how the waves interact with electrons due to the changing wave properties, especially nonlinear interactions, and thereby influences the energy transfer between whistler waves and electrons (Artemyev et al., 2016; Hsieh et al., 2020, 2022; Kang et al., 2024; Ke, Gao et al., 2022a; Ke, Lu, , 2024). For instance, in comparison with parallel (or ducted) whistler waves, oblique whistler waves can easily accelerate energetic electrons through Landau resonance and thus decay significantly (Artemyev et al., 2013; Gan et al., 2023; Hsieh & Omura, 2018; Kang et al., 2024; Shen et al., 2021). Therefore, unraveling the propagation characteristics of whistler waves has implications for comprehending the dynamic evolution of radiation belt electrons.

Ray-tracing and full-wave models have been widely applied to investigate whistler wave propagation in the Earth's magnetosphere (Bortnik et al., 2007; Katoh, 2014; Ke, Lu, et al., 2022; Xu et al., 2020). Full-wave models ignore resonant interactions. Ray-tracing models, in combination with the linear theory, can describe the linear evolution of the waves along the propagation path (Brinca, 1972; L. Chen et al., 2013; Kang et al., 2021). However, ray-tracing models neither include nonlinear resonant interactions nor involve the variations of particle distributions, which are also crucial for the wave evolution and thus require kinetic simulation models. In recent years, several two-dimensional (2-D) kinetic simulation models have been developed to investigate the generation and propagation of whistler waves (Lu et al., 2019; Silva et al., 2017; Wang et al., 2024; Wu et al., 2015). Nevertheless, detailed and quantitative analyses of the nonlinear evolution of whistler waves remain scarce. In this study, we utilize the 2-D gcPIC simulation model to simulate the propagation of whistler waves, quantify the wave evolution, and compare the results with ray-tracing simulations.

2. Simulation Model

A 2-D gcPIC simulation model (Lu et al., 2019) was utilized to investigate the propagation of whistler waves in the Earth's magnetosphere. In the simulation model, a monochromatic whistler wave was launched at the magnetic equator in a dipole magnetic field, and the hot electrons were set to have a lower temperature anisotropy. Under these conditions, these hot electrons cannot excite whistler waves self-consistently, and the pump whistler wave is also unable to trigger chorus waves with frequency chirping. This study focuses on the propagation of whistler waves and their nonlinear damping, rather than nonlinear growth.

In our simulation system, the plasma consists of fixed protons, cold electrons, and hot electrons. The cold electrons are regarded as a fluid, while the hot electrons are treated as particles. Initially, the cold electron fluid has a uniform distribution, with a number density of n_0 and a bulk velocity of zero. The hot electrons, subject to a bi-Maxwellian distribution, have a temperature anisotropy of $T_{\perp eq}/T_{\parallel eq} = 1.7$, and a number density of $n_{heq}/n_0 = 0.02$ at the magnetic equator. The parallel thermal velocity of hot electrons is $v_{th}/c = 0.1$ (where c is the speed of light). We use a simulation domain of $x_{eq}/d_{e0} = 1950 - 2050$ (where x_{eq} is x at the equator and $d_{e0} = c/\omega_{pe}$) in the magnetic meridian plane, within the magnetic latitude range of $|\lambda| \leq \sim 20^\circ$. The ratio of the electron plasma frequency ω_{pe} to the electron gyrofrequency Ω_{e0} is $\omega_{pe}/\Omega_{e0} = 5$, which is a typical value in the Earth's inner magnetosphere especially at $L \approx 6$. Here, $\Omega_{e0} = \frac{eB_{0eq,m}}{m_e}$, and $B_{0eq,m}$ is the background magnetic field at the central location ($x = 2000d_{e0}$, $\lambda = 0^\circ$). Actually, the electron inertia length $d_{e0} = c/\omega_{pe}$ is usually a few kilometers (km) at $L \approx 6$ in the Earth's inner magnetosphere. Thus, $L \approx 6$ corresponds to $\sim 10,000 d_{e0}$. We use a scaled-down simulation domain ($x_{eq}/d_{e0} \approx 2000$) to save computational time.

A parallel whistler wave with a frequency of $\omega/\Omega_{e0} = 0.4$ (or 0.35) is launched from an equatorial source region at $x_{eq}/d_{e0} = 1970 - 2030$ during the time interval of $\Omega_{e0}t = 0 - 700$. The wave amplitude remains constant $B_w = B_{w0}$ during $\Omega_{e0}t = 100 - 600$, and increases from 0 to B_{w0} following a hyperbolic sine function within $\Omega_{e0}t = 0 - 100$, and decreases from B_{w0} to 0 following the similar function within $\Omega_{e0}t = 600 - 700$. $B_{w0}/B_{0eq,m}$ in particle-in-cell (PIC) simulation Runs 1–3 are 0.02, 0.04, and 0.06 respectively. In our simulations, the boundary conditions for waves are absorbing, and those for particles are reflecting. The grid numbers are $N_{\parallel} \times N_{\perp} = 4000 \times 300$, the time step is $\Omega_{e0} \Delta t = 0.04$, and the number of particles per cell is about 2,000. A 2-D ray-tracing model (Ke, Lu, et al., 2022) has also been employed to describe the propagation of such whistler wave for comparison with the PIC simulation results.

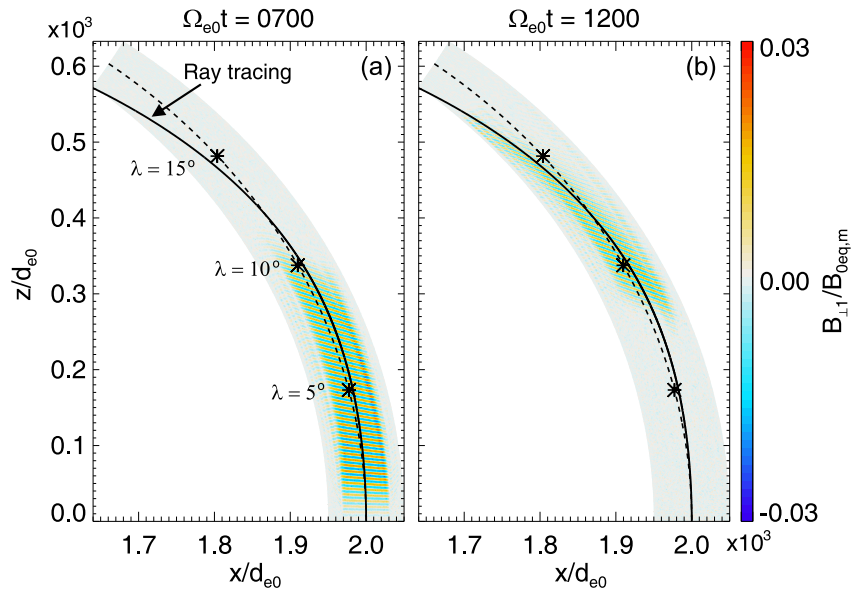


Figure 1. (a), (b) Spatial profiles of the perpendicular magnetic component $B_{\perp 1}$ of the whistler wave with $\omega/\Omega_{e0} = 0.4$ at $\Omega_{e0}t = 700$ and $1,200$ in Run 1. The dotted and solid lines denote the middle magnetic field line and the raypath of such a whistler wave emitting from the central location. Three asterisks mark the magnetic latitudes of $\lambda = 5^\circ, 10^\circ,$ and 15° .

3. Simulation Results

Figure 1 presents an overview of the propagation of the whistler wave with $\omega/\Omega_{e0} = 0.4$ in a dipole magnetic field in simulation Run 1. Figures 1a and 1b show the spatial profiles of the perpendicular magnetic component $B_{\perp 1}$ (perpendicular to the simulation plane) of this whistler wave at $\Omega_{e0}t = 700$ and $1,200$. Evidently, the whistler wave packet propagates from the equator to $\lambda \approx 15^\circ$ almost along the magnetic field lines (dotted line). Its propagation path is highly consistent with the wave raypath (solid line) given by the ray-tracing model. In addition, the wave packet normal is quasi-parallel to the background magnetic field \mathbf{B}_0 near the equator, but has a large angle with \mathbf{B}_0 at high latitude. The wave normal angles (WNAs) θ of the wave packet are calculated along the solid line, which are almost identical to those given by the ray-tracing model (shown in Figure 2). The WNAs increase with the increase of the magnetic latitude, reaching $\sim 60^\circ$ at $\lambda = 15^\circ$. The resonance cone angle is much larger than the WNA at $\lambda < 15^\circ$, reaching $\sim 73^\circ$ at $\lambda = 15^\circ$. The Gendrin angle increases from $\sim 37^\circ$ to $\sim 55^\circ$ when the wave propagates from $\lambda = 0^\circ$ to $\lambda = 15^\circ$. Furthermore, the waveform indicates that the wavelength of the whistler wave becomes shorter at higher latitudes, which is consistent with the dispersion relationship of whistler waves. In both the PIC and ray-tracing simulations, the propagation paths and WNAs of the whistler wave display a nearly identical pattern.

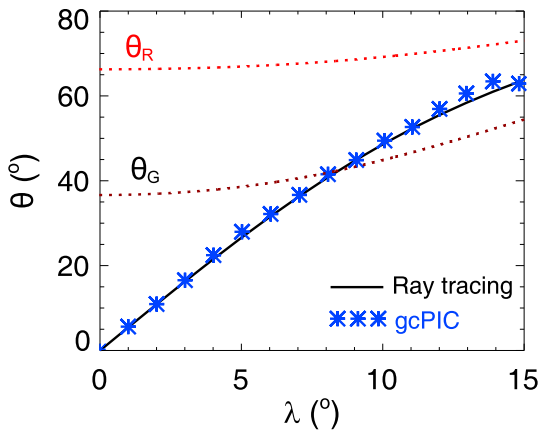


Figure 2. The wave normal angles (WNAs) θ along the raypath in the ray-tracing simulation (the solid line) and in the PIC simulation Run 1 (the asterisk line). The Gendrin and resonance cone angles (θ_G and θ_R) are marked by black and red dotted lines. In PIC simulations, θ is estimated as the average WNA of the waveform with the initial amplitude B_{w0} .

However, there is a significant difference in the amplitude evolution of the whistler wave between the two types of simulations. In the ray-tracing simulation, the linear growth rate is estimated using the initial electron distribution, which is assumed to remain constant in subsequent evolution. In Figure 3a, the relative magnetic amplitude B_w/B_{w0} of the whistler wave is calculated along the wave raypath (shown in Figure 1) in the ray-tracing simulation, as well as in each PIC simulation Run. Additionally, the change rate of the relative amplitude B_w/B_{w0} with respect to the magnetic latitude λ is also obtained and presented in Figure 3b. In the ray-tracing simulation, the relative amplitude B_w/B_{w0} gradually reduces as the latitude λ rises (the dotted line in Figure 3a), meanwhile, the change rate of B_w/B_{w0} with respect to λ gradually increases and saturates at $\lambda \approx 13^\circ$ (the dotted line in Figure 3b). Here, the relative amplitude is evaluated by integrating the local linear growth

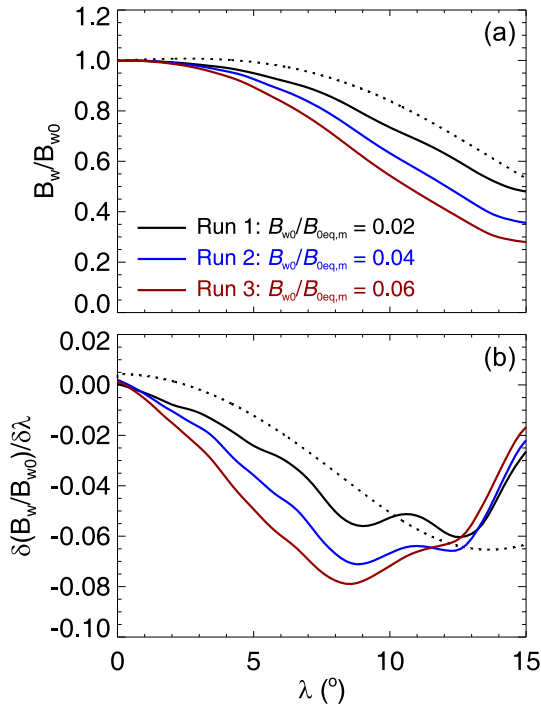


Figure 3. (a) The relative magnetic amplitude B_w/B_{w0} of the whistler wave with $\omega/\Omega_{e0} = 0.4$ along the wave raypath in the ray-tracing simulation (the dotted line) and in PIC simulation Runs 1–3, and (b) the change rate of B_w/B_{w0} with respect to the magnetic latitude λ . Here, B_w is estimated as the average magnetic amplitude of the waveform with the initial amplitude B_{w0} .

rate of the wave along its raypath. In PIC simulation Runs 1–3, the relative amplitude B_w/B_{w0} of the whistler wave also gradually reduces with the increase of λ , but the drop of B_w/B_{w0} is greater than that in the ray-tracing simulation at $\lambda \leq 15^\circ$, and the larger the initial amplitude B_{w0} , the greater the drop (Figure 3a). At lower latitudes ($\lambda < \sim 9^\circ$), the change rate of B_w/B_{w0} with respect to λ also gradually increases but increases more rapidly than that in the ray-tracing simulation, and as the initial amplitude B_{w0} becomes larger, the change rate becomes greater. Unexpectedly, at higher latitudes, the change rate $\delta(B_w/B_{w0})/\delta\lambda$ starts to decrease and drops rapidly when $\lambda > 12.5^\circ$, and the change rate is even smaller than that in the ray-tracing simulation at $\lambda > 12.5^\circ$ (Figure 3b).

To further explain the wave amplitude evolution, we calculate the linear growth rate in the ray-tracing simulation as well as the dot product of the current density \mathbf{J} and the wave electric field \mathbf{E} in each PIC simulation, and present the results in Figure 4. In our simulations, we assume a lower temperature anisotropy of hot electrons, which causes the linear cyclotron growth rate γ_G (the gold line) of the wave to be close to 0. Moreover, the linear Landau damping rate γ_L (the black line) of the wave increases as the latitude λ rises since the wave gradually becomes oblique (Figure 4a). In addition, the linear growth rates of anomalous and second-order cyclotron resonances ($m = -1, 2$) are almost zero, which are ignored in our ray-tracing results. The power dissipation of $\mathbf{J} \cdot \mathbf{E}$ represents the energy transfer between the whistler wave and the electrons. We only show the perpendicular components of $\mathbf{J} \cdot \mathbf{E}$ because $\mathbf{J}_{\parallel} \cdot \mathbf{E}_{\parallel}$ is nearly zero in our PIC simulations, which is consistent with previous simulation work (Hsieh & Omura, 2018). Figures 4b and 4c presents $\mathbf{J}_{\perp}^{-} \cdot \mathbf{E}_{\perp}$ ($\mathbf{J}_{\perp}^{+} \cdot \mathbf{E}_{\perp}$) along the wave raypath in PIC simulations, where \mathbf{E}_{\perp} is the perpendicular electric field of the wave, normalized by its initial electric field amplitude E_{w0} . Here, \mathbf{J}_{\perp}^{-} (\mathbf{J}_{\perp}^{+}) is the perpendicular component of current

density contributed by the electrons moving equatorward (poleward), in the unit of $J_0 = en_0 V_{Ae}$ (where $V_{Ae} = B_{0eq,m}/\sqrt{\mu_0 n_0 m_e}$). Generally, $\mathbf{J}_{\perp}^{-} \cdot \mathbf{E}_{\perp}$ is mainly contributed by the cyclotron resonance. The contribution of the anomalous cyclotron resonance is included in $\mathbf{J}_{\perp}^{+} \cdot \mathbf{E}_{\perp}$, but its resonant velocity $v_{m=-1} = (\omega + \Omega_e)/k_{\parallel}$ is more than three times the Landau resonant velocity $v_L = \omega/k_{\parallel}$. As a result, the value of $\mathbf{J}_{\perp}^{+} \cdot \mathbf{E}_{\perp}$ ($v_{\parallel} > v_{m=-1} - v_L$) has been estimated and is close to zero. Therefore, the Landau resonance primarily contributes to $\mathbf{J}_{\perp}^{+} \cdot \mathbf{E}_{\perp}$. Besides, we artificially add magnetic perturbations in the form of a whistler mode at the equator to trigger whistler eigenmodes, which then propagate toward the north and south poles. The artificial wave source leads to large $\mathbf{J}_{\perp}^{+} \cdot \mathbf{E}_{\perp}$ around the equator. This study mainly focuses on the propagation of whistler waves off the equator. Thus, Figure 4 only shows $\mathbf{J} \cdot \mathbf{E}$ at the latitude $\lambda \geq 1^\circ$.

At lower latitudes, $\mathbf{J}_{\perp}^{-} \cdot \mathbf{E}_{\perp}$ is mainly positive in Runs 1–3, and as the initial amplitude B_{w0} of the wave becomes larger, $\mathbf{J}_{\perp}^{-} \cdot \mathbf{E}_{\perp}$ becomes greater, which suggests that nonlinear cyclotron resonance contributes more to the wave damping for the stronger whistler wave. However, at higher latitudes, $\mathbf{J}_{\perp}^{-} \cdot \mathbf{E}_{\perp}$ is mainly negative in Runs 1–3, but it is close to 0 in Runs 2 and 3 (Figure 4b). In Figure 4c, $\mathbf{J}_{\perp}^{+} \cdot \mathbf{E}_{\perp}$ is mainly positive, and it first gradually rises and then rapidly drops, reaching the peak at $\lambda \approx 11^\circ$ in each Run. This indicates that the Landau damping of the wave gradually increases at lower latitudes and then decreases rapidly at higher latitudes. Interestingly, as the initial amplitude B_{w0} of the wave becomes larger, $\mathbf{J}_{\perp}^{+} \cdot \mathbf{E}_{\perp}$ becomes greater at lower latitudes but becomes smaller at higher latitudes. This result suggests that the stronger whistler wave experiences greater nonlinear Landau damping at lower latitudes. Based on the analysis of $\mathbf{J} \cdot \mathbf{E}$, we can conclude that the amplitude of the whistler wave undergoes greater attenuation at lower latitudes because of nonlinear cyclotron and Landau resonances, and undergoes weaker attenuation at higher latitudes mainly due to weaker Landau damping.

At higher latitudes, the variation in the hot electron distribution is mainly responsible for the less damping of the whistler wave. Figure 5 shows the parallel velocity distributions of hot electrons (the blue lines) at $\lambda = 5^\circ, 10^\circ$, and 13° at $\Omega_{e0}t = 700, 1,100$, and $1,300$ respectively in Run 2. These selected times are the moments when the wave passes through these latitudes. Compared with the initial parallel velocity distribution function f_0 (the black

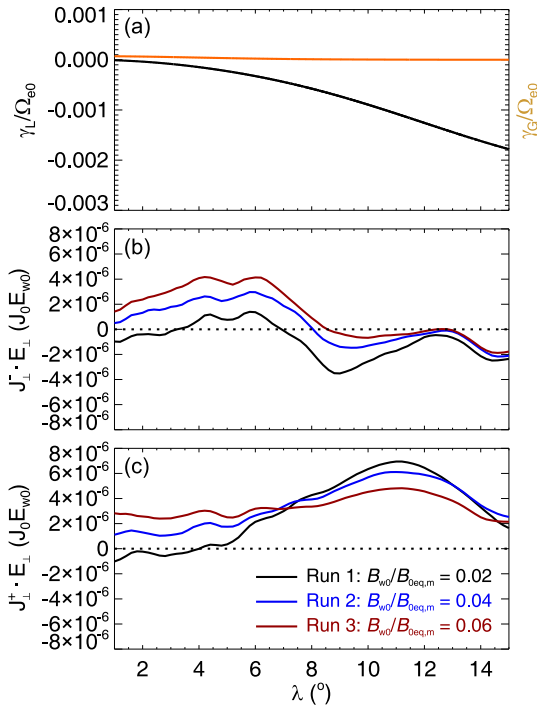


Figure 4. (a) The linear cyclotron growth rate (the gold line) and the linear Landau damping rate (the black line) of the whistler wave in the ray-tracing simulation, and (b) $J_{\perp}^{-} \cdot E_{\perp}^{-}$ and (c) $J_{\perp}^{+} \cdot E_{\perp}^{+}$ along the wave raypath in PIC simulation Runs 1–3. J_{\perp}^{-} (J_{\perp}^{+}) is contributed by the electrons moving equatorward (poleward).

line), the variations of the parallel velocity distribution function f mainly take place near the Landau resonant velocity v_L . The variations of the function f are minor at $\lambda = 5^{\circ}$ (Figure 5a), whereas a plateau distribution appears near v_L at $\lambda = 10^{\circ}$ (Figure 5b). When the whistler wave passes through $\lambda = 13^{\circ}$, a beam distribution occurs at around v_L (Figure 5c). The WNA θ of the wave is about 58° at $\lambda = 13^{\circ}$. The occurrence of the electron plateau and beam distributions in the parallel velocity contributes to the slowdown of the wave damping at higher latitudes. According to the linear theory, the linear Landau damping rates γ_L of the whistler waves with $\theta \approx 58^{\circ}$ at $\omega/\Omega_{e0} \approx 0.25 - 0.4$ are estimated based on the initial electron distribution and the electron distribution at $\Omega_{e0}t = 1,300$ at $\lambda = 13^{\circ}$. The linear Landau damping rates under the electron distribution with beam populations are about 30%–40% of those under the initial distribution (Figure 5d).

In order to investigate the formation mechanism of the plateau/beam distribution, we track the trajectories of the beam electron component with $|v_{\parallel} - v_L|/V_{Ae} < 0.1$ at $\lambda = 13^{\circ}$ in Run 2 (Figure 5c), and find that these electrons can be classified into two groups: trapped electrons and untrapped electrons. The parallel velocities v_{\parallel} , the kinetic energies E_k , and the pitch angles (PA) of a trapped electron and an untrapped electron in Run 2 are presented in Figure 6. The dotted line marks the Landau resonant velocity v_L . This trapped electron is Landau-resonantly trapped by the whistler wave from near the equator to higher latitudes. Meanwhile, its parallel velocity fluctuates around the line of Landau resonant velocity, its kinetic energy increases from ~ 7.5 to ~ 10 keV, and its PA fluctuates and decreases slightly. This untrapped electron only resonates with the whistler wave briefly. Its parallel velocity gradually decreases as the latitude increases and satisfies the Landau resonant condition at $\lambda \approx 13^{\circ}$. Its kinetic energy remains nearly constant, and its PA increases as the latitude increases. Interestingly, $\sim 70\%$ of these electrons with

$|v_{\parallel} - v_L|/V_{Ae} < 0.1$ are trapped electrons. The proportion drops to less than 50% for electrons with $|v_{\parallel} - v_L|/V_{Ae} < 0.2$. Although trapped electrons get energy from the wave, untrapped (especially phase bunched) electrons tend to provide energy to the wave (Artemyev et al., 2014). Therefore, nonlinear Landau resonances form the electron beam distribution, as well as the electron plateau distribution, which in turn inhibit Landau damping of the wave at higher latitudes.

To verify the generality of the results, we conducted another PIC simulation (Run 4) with the frequency of the whistler wave set as $\omega/\Omega_{e0} = 0.35$. Figures 7a and 7b show the spatial profiles of the perpendicular magnetic component $B_{\perp 1}$ of this whistler wave at $\Omega_{e0}t = 700$ and 1,200. During its propagation, the waveform first deviates

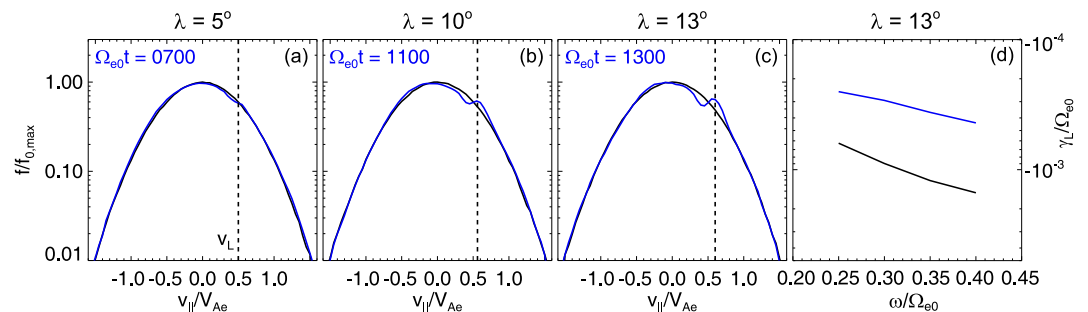


Figure 5. (a–c) The parallel velocity distributions of hot electrons (the blue lines) at $\lambda = 5^{\circ}$, 10° , and 13° at $\Omega_{e0}t = 700$, 1,100, and 1,300 respectively in Run 2. The black line indicates the initial parallel velocity distribution function f_0 in each panel. $f_{0,max}$ is the maximum value of the function f_0 . The dotted line marks the local Landau resonant velocity v_L , and (d) the linear Landau damping rate of whistler waves with $\theta \approx 58^{\circ}$ based on the initial electron distribution (the black line) and the electron distribution at $\Omega_{e0}t = 1,300$ (the blue line) at $\lambda = 13^{\circ}$.

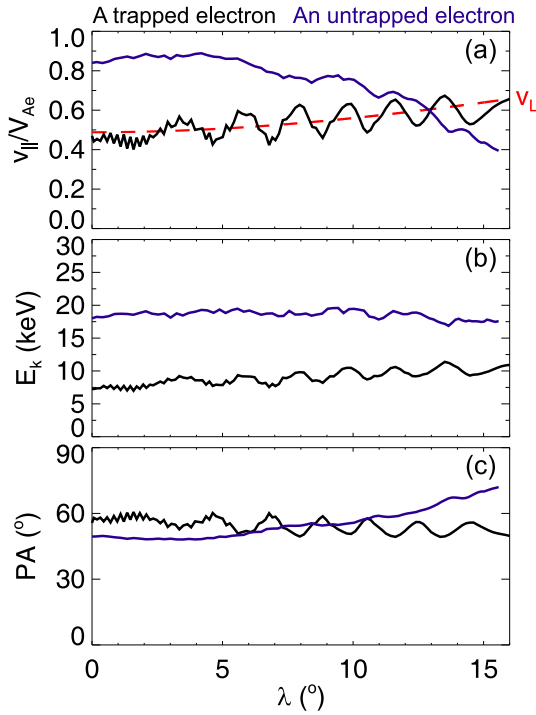


Figure 6. (a–c) The parallel velocities $v_{||}$, the kinetic energies E_k , and the pitch angles PA of a trapped electron and an untrapped electron in Run 2. The dotted line marks the Landau resonant velocity v_L .

slightly outward before deviating inward. The propagation path of the waveform is consistent with the raypath given by the ray-tracing simulation. The WNAs in the two simulations also closely match (not shown). Figures 7c and 7d display the relative magnetic amplitude B_w/B_{w0} of this whistler wave along the wave raypath and the change rate of B_w/B_{w0} with respect to λ , respectively. Specifically, the dotted lines represent the results in the ray-tracing simulation, while the solid lines stand for those in the PIC simulation. Compared with the results in the ray-tracing simulation, in the PIC simulation (Run 4), the whistler wave decays more significantly at lower latitudes, but the wave damping rate reduces rapidly at higher latitudes. These results are similar to those in PIC simulation Runs 1–3.

4. Conclusions and Discussion

In this study, two-dimensional (2-D) gcPIC simulations have been carried out to study the propagation of a whistler wave in a dipole magnetic field. The propagation characteristics of the whistle wave are quantitatively calculated and compared with the ray-tracing simulation results. During its propagation, the amplitude evolution of the whistler wave in PIC simulations differs significantly from that in ray-tracing simulations. The primary conclusions are summarized as follows.

1. Both the PIC and ray-tracing simulation models display a nearly identical pattern of the propagation path and WNA of a whistler wave in a dipole magnetic field.
2. At lower magnetic latitudes, the whistler wave in the PIC simulation experiences greater damping than that in the ray-tracing simulation due to nonlinear Landau and cyclotron resonances, especially for the stronger whistler wave.
3. At higher magnetic latitudes, the whistler wave in the PIC simulation undergoes weaker damping than that in the ray-tracing simulation because of the electron plateau/beam distributions formed by Landau trapping of the whistler wave.

Previous observational and simulation studies have also shown that the oblique propagation of whistler waves can lead to electron plateau/beam distributions in the parallel velocity (Agapitov et al., 2015; Ke, Gao, et al., 2022; Wu et al., 2024). However, the influence of these distributions in turn on the evolution of these waves has not been studied thoroughly. Some other studies have shown that the electron plateau/beam distributions in the parallel

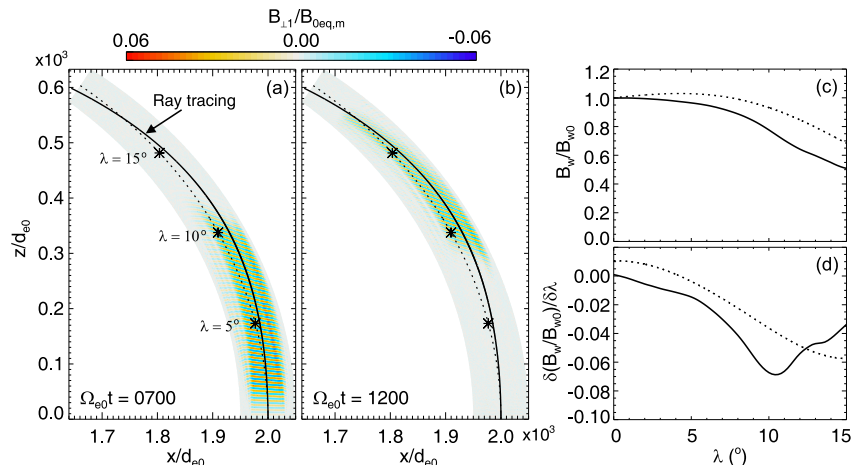


Figure 7. (a), (b) Spatial profiles of the perpendicular magnetic component $B_{\perp 1}$ of the whistler wave with $\omega/\Omega_{e0} = 0.35$ at $\Omega_{e0}t = 700$ and $1,200$ in Run 4, (c), and (d) are similar to Figures 3a and 3b.

velocity play a key role in the excitation and propagation of oblique whistler waves by suppressing Landau damping (Li et al., 2016; Ma et al., 2017; Mourenas et al., 2015), but their sources have not been elucidated (Artemyev & Mourenas, 2020). However, in contrast to these previous studies, our simulations demonstrate that nonlinear Landau trapping of the whistler wave forms the electron plateau/beam distributions, which in turn inhibit Landau damping of the wave at higher latitudes.

In this study, we focus on the propagation of a whistler wave and the wave damping during its propagation. Thus, we assume a relatively low temperature anisotropy of hot electrons in our simulation models, which leads to a nearly zero linear cyclotron growth rate. Nevertheless, nonlinear cyclotron resonances contribute to the wave damping at lower latitudes for stronger whistler waves in our PIC simulations. The whistler wave may trigger rising-tone chorus waves when the temperature anisotropy of hot electrons becomes larger, and in this case, nonlinear cyclotron resonances contribute to the wave growth. This situation will be explored by our 2-D gcPIC simulations in the future.

In our PIC simulations, we only simulate lower-band waves within $|\lambda| \leq 20^\circ$ due to limited computational resources. We present the wave evolution within $|\lambda| \leq 15^\circ$ because of the absorbing boundary conditions for waves. Once the wave reaches higher latitudes, its wavelength λ_w tends to become smaller. For instance, the wave with $\omega/\Omega_{e0} = 0.4$ has $\lambda_w = 7.66d_{e0}$ at $\lambda = 0^\circ$ and $\lambda_w = 4.43d_{e0}$ at $\lambda = 15^\circ$ in our simulations. Therefore, the simulation of whistler waves at higher latitudes requires smaller grid spacing. Moreover, the upper-band waves have shorter wavelengths, necessitating smaller grid spacing. Their propagation paths deviate more from the original magnetic field lines, requiring a larger simulation domain. When sufficient computing resources are available, the whistler wave at higher frequency and higher latitudes will be simulated in the future.

Data Availability Statement

The simulation data used to plot the figures are available at National Space Science Data Center, National Science and Technology Infrastructure of China via Y. Ke (2025).

Acknowledgments

This research was funded by the National Science Foundation of China (NSFC) Grants 42230201, 42474202, 42322406. Computer resources were provided by the Hefei Advanced Computing Center of China.

References

- Agapitov, O., Artemyev, A., Krasnoselskikh, V., Khotyaintsev, Y. V., Mourenas, D., Breuillard, H., et al. (2013). Statistics of whistler mode waves in the outer radiation belt: Cluster STAFF-SA measurements. *Journal of Geophysical Research: Space Physics*, *118*(6), 3407–3420. <https://doi.org/10.1002/jgra.50312>
- Agapitov, O., Artemyev, A. V., Mourenas, D., Mozer, F. S., & Krasnoselskikh, V. (2015). Nonlinear local parallel acceleration of electrons through Landau trapping by oblique whistler mode waves in the outer radiation belt. *Geophysical Research Letters*, *42*(23), 10140–110149. <https://doi.org/10.1002/2015gl066887>
- Agapitov, O., Krasnoselskikh, V., Khotyaintsev, Y. V., & Rolland, G. (2011). A statistical study of the propagation characteristics of whistler waves observed by Cluster. *Geophysical Research Letters*, *38*(20), L20103. <https://doi.org/10.1029/2011GL049597>
- Anderson, R. R., & Maeda, K. (1977). VLF emissions associated with enhanced magnetospheric electrons. *Journal of Geophysical Research*, *82*(1), 135–146. <https://doi.org/10.1029/JA082i001p00135>
- Artemyev, A., Agapitov, O., Mourenas, D., Krasnoselskikh, V., Shastun, V., & Mozer, F. (2016). Oblique whistler-mode waves in the earth's inner magnetosphere: Energy distribution, origins, and role in radiation belt dynamics. *Space Science Reviews*, *200*(1–4), 261–355. <https://doi.org/10.1007/s11214-016-0252-5>
- Artemyev, A. V., & Mourenas, D. (2020). On whistler mode wave relation to electron field-aligned plateau populations. *Journal of Geophysical Research: Space Physics*, *125*(3), e2019JA027735. <https://doi.org/10.1029/2019JA027735>
- Artemyev, A. V., Vasiliev, A. A., Mourenas, D., Agapitov, O. V., Krasnoselskikh, V., Boscher, D., & Rolland, G. (2014). Fast transport of resonant electrons in phase space due to nonlinear trapping by whistler waves. *Geophysical Research Letters*, *41*(16), 5727–5733. <https://doi.org/10.1002/2014GL061380>
- Artemyev, A. V., Vasiliev, A. A., Mourenas, D., Agapitov, O. V., & Krasnoselskikh, V. V. (2013). Nonlinear electron acceleration by oblique whistler waves: Landau resonance vs. cyclotron resonance. *Physics of Plasmas*, *20*(12), 122901. <https://doi.org/10.1063/1.4836595>
- Bortnik, J., & Thorne, R. M. (2007). The dual role of ELF/VLF chorus waves in the acceleration and precipitation of radiation belt electrons. *Journal of Atmospheric and Solar-Terrestrial Physics*, *69*(3), 378–386. <https://doi.org/10.1016/j.jastp.2006.05.030>
- Bortnik, J., Thorne, R. M., & Meredith, N. P. (2007). Modeling the propagation characteristics of chorus using CRRES suprathermal electron fluxes. *Journal of Geophysical Research*, *112*(A8), A08204. <https://doi.org/10.1029/2006JA012237>
- Breuillard, H., Zaliznyak, Y., Krasnoselskikh, V., Agapitov, O., Artemyev, A., & Rolland, G. (2012). Chorus wave-normal statistics in the Earth's radiation belts from ray tracing technique. *Annales Geophysicae*, *30*(8), 1223–1233. <https://doi.org/10.5194/angeo-30-1223-2012>
- Brinca, A. L. (1972). On the stability of obliquely propagating whistlers. *Journal of Geophysical Research*, *77*(19), 3495–3507. <https://doi.org/10.1029/JA077i019p03495>
- Chen, H., Gao, X., Lu, Q., Sauer, K., Chen, R., Yao, J., & Wang, S. (2021). Gap Formation around 0.5 Ω_e of whistler-mode waves excited by electron temperature anisotropy. *Journal of Geophysical Research: Space Physics*, *126*(2), e2020JA028631. <https://doi.org/10.1029/2020ja028631>
- Chen, L., Thorne, R. M., Li, W., & Bortnik, J. (2013). Modeling the wave normal distribution of chorus waves. *Journal of Geophysical Research: Space Physics*, *118*(3), 1074–1088. <https://doi.org/10.1029/2012ja018343>

- Chen, R., Gao, X., Lu, Q., Chen, L., Tsurutani, B. T., Li, W., et al. (2021). In situ observations of whistler-mode chorus waves guided by density ducts. *Journal of Geophysical Research: Space Physics*, *126*(4), e2020JA028814. <https://doi.org/10.1029/2020JA028814>
- Fu, X., Cowee, M. M., Friedel, R. H., Funsten, H. O., Gary, S. P., Hospodarsky, G. B., et al. (2014). Whistler anisotropy instabilities as the source of banded chorus: Van Allen Probes observations and particle-in-cell simulations. *Journal of Geophysical Research: Space Physics*, *119*(10), 8288–8298. <https://doi.org/10.1002/2014JA020364>
- Gan, L., Artemyev, A., Li, W., Zhang, X.-J., Ma, Q., Mourenas, D., et al. (2023). Bursty energetic electron precipitation by high-order resonance with very-oblique whistler-mode waves. *Geophysical Research Letters*, *50*(8), e2022GL101920. <https://doi.org/10.1029/2022GL101920>
- Gao, X., Chen, L., Li, W., Lu, Q., & Wang, S. (2019). Statistical results of the power gap between lower-band and upper-band chorus waves. *Geophysical Research Letters*, *46*(8), 4098–4105. <https://doi.org/10.1029/2019gl082140>
- Gao, X., Chen, R., Lu, Q., Chen, L., Chen, H., & Wang, X. (2022). Observational evidence for the origin of repetitive chorus emissions. *Geophysical Research Letters*, *49*(12), e2022GL099000. <https://doi.org/10.1029/2022GL099000>
- Gao, X., Ma, J., Shao, T., Chen, R., Ke, Y., & Lu, Q. (2023). Why chorus waves are the dominant driver for diffuse auroral precipitation. *Science Bulletin*, *69*(5), 597–600. <https://doi.org/10.1016/j.scib.2023.12.009>
- Hanzelka, M., & Santolik, O. (2019). Effects of ducting on whistler mode chorus or exohiss in the outer radiation belt. *Geophysical Research Letters*, *46*(11), 5735–5745. <https://doi.org/10.1029/2017gl083115>
- Horne, R. B., Thorne, R. M., Glauert, S. A., Albert, J. M., Meredith, N. P., & Anderson, R. R. (2005). Timescale for radiation belt electron acceleration by whistler mode chorus waves. *Journal of Geophysical Research*, *110*(A3), A03225. <https://doi.org/10.1029/2004JA010811>
- Hsieh, Y.-K., Kubota, Y., & Omura, Y. (2020). Nonlinear evolution of radiation belt electron fluxes interacting with oblique whistler mode chorus emissions. *Journal of Geophysical Research: Space Physics*, *125*(2), e2019JA027465. <https://doi.org/10.1029/2019JA027465>
- Hsieh, Y.-K., & Omura, Y. (2018). Nonlinear damping of oblique whistler mode waves via Landau resonance. *Journal of Geophysical Research: Space Physics*, *123*(9), 7462–7472. <https://doi.org/10.1029/2018JA025848>
- Hsieh, Y.-K., Omura, Y., & Kubota, Y. (2022). Energetic electron precipitation induced by oblique whistler mode chorus emissions. *Journal of Geophysical Research: Space Physics*, *127*(1), e2021JA029583. <https://doi.org/10.1029/2021JA029583>
- Kang, N., Artemyev, A. V., Bortnik, J., Zhang, X.-J., & Angelopoulos, V. (2024). The Principal role of chorus ducting for night-side relativistic electron precipitation. *Geophysical Research Letters*, *51*(17), e2024GL110365. <https://doi.org/10.1029/2024GL110365>
- Kang, N., Bortnik, J., An, X., & Claudepierre, S. G. (2021). Propagation of chorus waves generated in minimum-B pockets. *Geophysical Research Letters*, *48*(24), e2021GL096478. <https://doi.org/10.1029/2021gl096478>
- Katoh, Y. (2014). A simulation study of the propagation of whistler-mode chorus in the Earth's inner magnetosphere. *Earth Planets and Space*, *66*(1), 1–12. <https://doi.org/10.1186/1880-5981-66-6>
- Ke, Y. (2025). Dataset for “whistler wave propagation in a dipole magnetic field: Two-dimensional gcPIC simulations” (Version 1) [Dataset]. *Science Data Bank*, 2001. <https://doi.org/10.57760/sciencedb.20145>
- Ke, Y., Chen, L., Gao, X., Lu, Q., Wang, X., Chen, R., et al. (2021). Whistler-mode waves trapped by density irregularities in the Earth's magnetosphere. *Geophysical Research Letters*, *48*(7), e2020GL092305. <https://doi.org/10.1029/2020GL092305>
- Ke, Y., Gao, X., Lu, Q., Wang, X., & Chen, R. (2024). Butterfly distributions of energetic electrons driven by ducted and nonducted chorus waves. *Geophysical Research Letters*, *51*(10), e2024GL108307. <https://doi.org/10.1029/2024GL108307>
- Ke, Y., Gao, X., Lu, Q., Wang, X., Chen, R., Chen, H., & Wang, S. (2022). Deformation of electron distributions due to Landau trapping by the whistler-mode wave. *Geophysical Research Letters*, *49*(3), e2021GL096428. <https://doi.org/10.1029/2021GL096428>
- Ke, Y., Gao, X., Lu, Q., Wang, X., & Wang, S. (2017). Generation of rising-tone chorus in a two-dimensional mirror field by using the general curvilinear PIC code. *Journal of Geophysical Research: Space Physics*, *122*(8), 8154–8165. <https://doi.org/10.1002/2017ja024178>
- Ke, Y., Lu, Q., Gao, X., Chen, H., & Chen, R. (2022). Ray-tracing simulations of whistler-mode wave propagation in different rescaled dipole magnetic fields. *Earth Planetary Physics*, *6*(6), 555–562. <https://doi.org/10.26464/epp2022048>
- Lauben, D. S., Inan, U. S., Bell, T. F., & Gurnett, D. A. (2002). Source characteristics of ELF/VLF chorus. *Journal of Geophysical Research*, *107*(A12), 1429. <https://doi.org/10.1029/2000JA003019>
- LeDocq, M. J., Gurnett, D. A., & Hospodarsky, G. B. (1998). Chorus source locations from VLF Poynting flux measurements with the Polar spacecraft. *Geophysical Research Letters*, *25*(21), 4063–4066. <https://doi.org/10.1029/1998GL900071>
- Li, W., Bortnik, J., Thorne, R. M., & Angelopoulos, V. (2011). Global distribution of wave amplitudes and wave normal angles of chorus waves using THEMIS wave observations. *Journal of Geophysical Research*, *116*(A12), A12205. <https://doi.org/10.1029/2011ja017035>
- Li, W., Mourenas, D., Artemyev, A. V., Bortnik, J., Thorne, R. M., Kletzing, C. A., et al. (2016). Unraveling the excitation mechanisms of highly oblique lower band chorus waves. *Geophysical Research Letters*, *43*(17), 8867–8875. <https://doi.org/10.1002/2016GL070386>
- Li, W., Thorne, R. M., Angelopoulos, V., Bortnik, J., Cully, C. M., Ni, B., et al. (2009). Global distribution of whistler-mode chorus waves observed on the THEMIS spacecraft. *Geophysical Research Letters*, *36*(9), 1–5. <https://doi.org/10.1029/2009GL037595>
- Li, W., Thorne, R. M., Bortnik, J., Tao, X., & Angelopoulos, V. (2012). Characteristics of hiss-like and discrete whistler-mode emissions. *Geophysical Research Letters*, *39*(18), L18106. <https://doi.org/10.1029/2012gl053206>
- Li, W., Thorne, R. M., Meredith, N. P., Home, R. B., Bortnik, J., Shprits, Y. Y., & Ni, B. (2008). Evaluation of whistler mode chorus amplification during an injection event observed on CRRES. *Journal of Geophysical Research*, *113*(9), 1–13. <https://doi.org/10.1029/2008JA013129>
- Lu, Q., Chen, L., Wang, X., Gao, X., Lin, Y., & Wang, S. (2021). Repetitive emissions of rising-tone chorus waves in the inner magnetosphere. *Geophysical Research Letters*, *48*(15), e2021GL094979. <https://doi.org/10.1029/2021GL094979>
- Lu, Q., Ke, Y., Wang, X., Liu, K., Gao, X., Chen, L., & Wang, S. (2019). Two-dimensional general curvilinear particle-in-cell (gcPIC) simulation of rising-tone chorus waves in a dipole magnetic field. *Journal of Geophysical Research: Space Physics*, *124*(6), 4157–4167. <https://doi.org/10.1029/2019JA026586>
- Ma, Q., Artemyev, A. V., Mourenas, D., Li, W., Thorne, R. M., Kletzing, C. A., et al. (2017). Very oblique whistler mode propagation in the radiation belts: Effects of hot plasma and Landau damping. *Geophysical Research Letters*, *44*(24), 12057–12066. <https://doi.org/10.1002/2017GL075892>
- Mourenas, D., Artemyev, A. V., Agapitov, O. V., Krasnoselskikh, V., & Mozer, F. S. (2015). Very oblique whistler generation by low-energy electron streams. *Journal of Geophysical Research: Space Physics*, *120*(5), 3665–3683. <https://doi.org/10.1002/2015JA021135>
- Ni, B., Thorne, R. M., Shprits, Y. Y., & Bortnik, J. (2008). Resonant scattering of plasma sheet electrons by whistler-mode chorus: Contribution to diffuse auroral precipitation. *Geophysical Research Letters*, *35*(11), L11106. <https://doi.org/10.1029/2008GL034032>
- Omura, Y., Hikishima, M., Katoh, Y., Summers, D., & Yagitani, S. (2009). Nonlinear mechanisms of lower-band and upper-band VLF chorus emissions in the magnetosphere. *Journal of Geophysical Research*, *114*(A7), A07217. <https://doi.org/10.1029/2009ja014206>
- Reeves, G. D., Spence, H. E., Henderson, M. G., Morley, S. K., Friedel, R. H. W., Funsten, H. O., et al. (2013). Electron acceleration in the heart of the Van Allen radiation belts. *Science*, *341*(6149), 991–994. <https://doi.org/10.1126/science.1237743>

- Santolík, O., Gurnett, D. A., Pickett, J. S., Parrot, M., & Cornilleau-Wehrin, N. (2005). Central position of the source region of storm-time chorus. *Planetary and Space Science*, 53(1–3), 299–305. <https://doi.org/10.1016/j.pss.2004.09.056>
- Santolík, O., Macušová, E., Kolmašová, I., Cornilleau-Wehrin, N., & de Conchy, Y. (2014). Propagation of lower-band whistler-mode waves in the outer Van Allen belt: Systematic analysis of 11 years of multi-component data from the Cluster spacecraft. *Geophysical Research Letters*, 41(8), 2729–2737. <https://doi.org/10.1002/2014GL059815>
- Shen, Y., Chen, L., Zhang, X.-J., Artemyev, A., Angelopoulos, V., Cully, C. M., et al. (2021). Conjugate observation of magnetospheric chorus propagating to the ionosphere by ducting. *Geophysical Research Letters*, 48(23), e2021GL095933. <https://doi.org/10.1029/2021GL095933>
- Silva, C. L., Wu, S., Denton, R. E., Hudson, M. K., & Millan, R. M. (2017). Hybrid fluid-particle simulation of whistler-mode waves in a compressed dipole magnetic field: Implications for dayside high-latitude chorus. *Journal of Geophysical Research: Space Physics*, 122(1), 432–448. <https://doi.org/10.1002/2016ja023446>
- Streltsov, A. V., & Bengtson, M. (2020). Observations and modeling of whistler-mode waves in the magnetospheric density ducts. *Journal of Geophysical Research: Space Physics*, 125(10), e2020JA028398. <https://doi.org/10.1029/2020JA028398>
- Summers, D., Ni, B., & Meredith, N. P. (2007). Timescales for radiation belt electron acceleration and loss due to resonant wave-particle interactions: 2. Evaluation for VLF chorus, ELF hiss, and electromagnetic ion cyclotron waves. *Journal of Geophysical Research*, 112(A4), A04207. <https://doi.org/10.1029/2006JA011993>
- Taubenschuss, U., Santolík, O., Breuillard, H., Li, W., & le Contel, O. (2016). Poynting vector and wave vector directions of equatorial chorus. *Journal of Geophysical Research: Space Physics*, 121(12), 11912–11928. <https://doi.org/10.1002/2016JA023389>
- Thorne, R. M., Li, W., Ni, B., Ma, Q., Bortnik, J., Chen, L., et al. (2013). Rapid local acceleration of relativistic radiation-belt electrons by magnetospheric chorus. *Nature*, 504(7480), 411–414. <https://doi.org/10.1038/Nature12889>
- Thorne, R. M., Ni, B., Tao, X., Horne, R. B., & Meredith, N. P. (2010). Scattering by chorus wave as the dominant cause of diffuse auroral precipitation. *Nature*, 467(7318), 943–946. <https://doi.org/10.1038/nature09467>
- Tsurutani, B. T., & Smith, E. J. (1974). Postmidnight chorus: A substorm phenomenon. *Journal of Geophysical Research*, 79(1), 118–127. <https://doi.org/10.1029/JA079i001p00118>
- Tsurutani, B. T., & Smith, E. J. (1977). Two types of magnetospheric ELF chorus and their substorm dependences. *Journal of Geophysical Research*, 82(32), 5112–5128. <https://doi.org/10.1029/JA082i032p05112>
- Wang, X., Chen, H., Omura, Y., Hsieh, Y.-K., Chen, L., Lin, Y., et al. (2024). Resonant electron signatures in the formation of chorus wave subpackets. *Geophysical Research Letters*, 51(8), e2023GL108000. <https://doi.org/10.1029/2023GL108000>
- Wu, S., Denton, R. E., Liu, K., & Hudson, M. K. (2015). One- and two-dimensional hybrid simulations of whistler mode waves in a dipole field. *Journal of Geophysical Research: Space Physics*, 120(3), 1908–1923. <https://doi.org/10.1002/2014JA020736>
- Wu, Y., Zhao, J., Tao, X., & Dai, L. (2024). Particle simulation study of obliquely propagating whistler waves in low-beta plasmas. *Journal of Geophysical Research: Space Physics*, 129(9), e2024JA033035. <https://doi.org/10.1029/2024JA033035>
- Xu, X., Chen, L., Zhou, C., Liu, X., Xia, Z., Simpson, J. J., & Zhang, Y. (2020). Two-dimensional full-wave simulation of whistler mode wave propagation near the local lower hybrid resonance frequency in a dipole field. *Journal of Geophysical Research: Space Physics*, 125(4), e2019JA027750. <https://doi.org/10.1029/2019JA027750>